ACS Chemical Neuroscience

pubs.acs.org/chemneuro Research Article

Melatonin-Induced Modulation of Cholesterol-Enriched Model Neuronal Membranes

Dima Bolmatov,* Russel J. Reiter, Dmitry Zav'yalov, Changwoo Do, Gergely Nagy, Charles Patrick Collier, John Katsaras, and Maxim O. Lavrentovich*

Cite This: https://doi.org/10.1021/acschemneuro.5c00682 Read Online

ACCESS | Metrics & More | Article Recommendations

ABSTRACT: Melatonin, a hormone primarily produced by the brain's pineal gland, not only regulates circadian rhythms, but also influences the structural and biophysical properties of neuronal membranes. Its amphiphilic nature enables direct incorporation into lipid bilayers and preferential interactions with cholesterol-rich lipid rafts, critical hubs for cellular signaling and membrane organization. Despite increasing recognition of its membrane activity, the molecular basis of melatonin's interactions with coexisting liquid-ordered (L_o) and liquid-disordered (L_d) phases remains unclear. Here, we combine small-angle neutron scattering (SANS) and all-atom molecular dynamics simulations to examine model neuronal membranes composed of DSPC, DOPC, POPC, and cholesterol. Our results show that melatonin preserves domain morphology while adopting distinct orientations within the bilayer and at the membrane interface, allowing both lateral and transmembrane bridging across lipid phases. These findings establish the molecular underpinnings of melatonin's modulation of membrane heterogeneity and provide strong support for its receptor-independent actions.

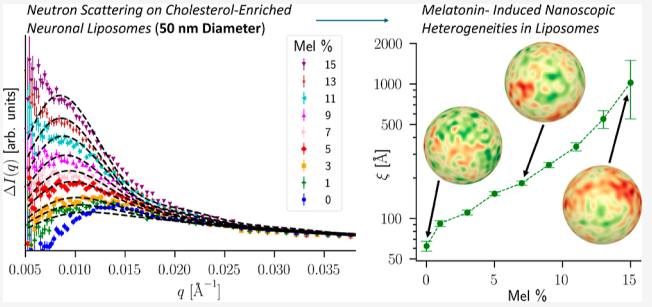

KEYWORDS: *neuronal membranes, phase separation, cholesterol, melatonin, neutron scattering, atomistic simulations*

1. INTRODUCTION

Melatonin, a neurohormone associated with circadian rhythm regulation, has recently gained recognition for its broader biological functions, including neuroprotection, antioxidant activity, and modulation of membrane structure.[1−3] While its receptor-mediated signaling pathways are well established,[4] melatonin's capacity to interact directly with lipid membranes—particularly those associated with the central nervous system (CNS)—has emerged as an alternative mechanism by which it may influence neuronal function.[4−7] Indeed, melatonin is not unique in this regard as its precursor, seratonin, is known to alter the mechanical properties of membranes,[5] with recent work indicating that these mechanical properties influence receptor activity, as well.[6] Although increasing evidence indicates that melatonin also alters membrane fluidity, thickness, and lipid order, the molecular basis of these effects remains poorly understood.

Neuronal membranes are complex structures, whose lipids are crucial structural and signaling components—lipids make up nearly 50% of the brain's dry weight.[7,8] These membranes are organized into dynamic, nanoscopic domains—commonly referred to as lipid rafts—that partition into coexisting liquid-ordered (L_o) and liquid-disordered (L_d) phases.[9,10] Enriched in cholesterol, sphingolipids, and membrane proteins, these microdomains serve as critical platforms for signal transduction, membrane trafficking, and spatial coordination of cellular processes.[11] Cholesterol, which constitutes approximately 40% of the lipid content in plasma membranes and myelin sheaths,[12] plays a central role in shaping domain architecture, lipid packing, and overall membrane physicochemical properties.[13] Disruption of cholesterol-rich domains has been implicated in the pathogenesis of neurodegenerative diseases such as Alzheimer's and Parkinson's.[14,15] Thus, understanding how melatonin interacts with nanoscopic lipid domains may, for example, reveal new physical pathways for neuroprotection.[16]

Melatonin's amphiphilic structure allows it to interact both with lipid headgroups and hydrophobic acyl chains, where it perturbs local order, modulates bilayer thickness, and interacts with cholesterol.[17,18] These interactions may influence phase behavior and domain organization within L_o/L_d-separated membranes.[19] However, the mechanisms by which melatonin alters membrane structure at the nanoscale remain currently

Received: August 26, 2025
Revised: February 3, 2026
Accepted: February 6, 2026

unresolved. Indeed, such interactions can be quite complex and lipid-composition-dependent, as demonstrated for seratonin.[20]

Here, we study melatonin's structural effects on phase-separated neuronal membrane mimics composed of DSPC, DOPC, POPC, and cholesterol. Using small-angle neutron scattering (SANS) and all-atom molecular dynamics (MD) simulations, we probe how melatonin modulates bilayer order, domain morphology, and lipid packing in coexisting L_o and L_d phases. Our results provide mechanistic insights into melatonin's role as a modulator of membrane heterogeneity and offer a physical framework for understanding its influence on neuronal membrane organization and membrane-associated functions.

2. METHODS

2.1. Materials

Lipids including 1,2-distearoyl-d_{70}-*sn*-glycero-3-phosphocholine (DSPC-d_{70}), 1,2-distearoyl-*sn*-glycero-3-phosphocholine (DSPC), 1,2-dioleoyl-*sn*-glycero-3-phosphocholine (DOPC), 1-palmitoyl-2-oleoyl-*sn*-glycero-3-phosphocholine (POPC), 1-palmitoyl-2-oleoyl-*sn*-glycero-3-phospho-(1′-*rac*-glycerol), and cholesterol were purchased from Avanti Polar Lipids (Alabaster, AL) as powders and used without further purification. Melatonin was purchased from Sigma-Aldrich (St. Louis, MO) and was used as received. A melatonin stock solution was prepared at a concentration of 10 mg/mL in trifluoroethanol (TFE; Sigma-Aldrich, St. Louis, MO). Stock solutions were stored at −80 °C until needed. Deionized water (H_2O) was obtained using a High-Q water purification system (Wilmette, IL).

2.2. Large Unilamellar Vesicle Preparation

Lipid stock solutions of DSPC-d_{70}, DSPC, DOPC, POPC, and cholesterol in a molar ratio of 0.255:0.135:0.06:0.33:0.22, respectively, were combined in glass vials and dissolved in chloroform. The solution was gently mixed by hand to ensure uniformity. Melatonin, dissolved in trifluoroethanol (TFE), was then added to the lipid mixture at varying molar percentages (1−15%, in increments of two). A control sample containing 0% melatonin was also prepared. The mixture was further homogenized, and the organic solvent was subsequently evaporated under a gentle stream of argon gas, followed by overnight drying under vacuum to remove residual solvents.

The resulting dry lipid film was hydrated with 34.6% D_2O at a temperature above the main phase transition of the lipid mixture. Hydration proceeded for at least 1 h with intermittent vortex mixing every 15 min. The resulting multilamellar vesicle (MLV) suspension underwent five freeze−thaw cycles between −80 °C and +50 °C to reduce multilamellarity and vesicle size. The MLVs were then extruded 31 times through a 50 nm pore diameter polycarbonate membrane using a Mini-Extruder (Avanti Polar Lipids, Alabaster, AL) preheated to 50 °C. The final lipid concentration was adjusted to 20 mg/mL.

2.3. Small Angle Neutron Scattering

The extended *Q*-range small-angle neutron diffractometer (EQ-SANS) at the Spallation Neutron Source at the Oak Ridge National Laboratory was used to characterize the lipid domain morphology.[21,22] Two sample-to-detector distances (2.5 and 4 m) were used with two wavelength bands defined by the minimum wavelength of λ_{min} = 0.25 nm and λ_{min} = 1 nm, respectively, to cover scattering wave vectors q ranging from 0.06 $nm^{-1} < q < 5$ nm^{-1}. The choppers were operated at 60 Hz. The vesicle solutions were loaded in the quartz cell of 2 mm path length and measured at 20 °C. The measured data were corrected by detector sensitivity and background scattering from the empty cell and then converted into absolute scale intensities using a porous silica standard sample.[23,24]

2.4. All-Atom Molecular Dynamics Details

The different systems consisted of 234 (DSPC), 198 (POPC), 36 (DOPC), and 132 (cholesterol) and melatonin (1−15 mol %) molecules. Approximately 23,000 water molecules were added to achieve full hydration. The system was assembled at Charm-Gui online service (https://charmm-gui.org).[25,26] The GROMACS software package and the CHARMM36m force field were used to perform MD simulations.[27,28]

The TIP3P model was used to simulate water molecules. Bond constraints were enforced using the LINCS algorithm. Lennard-Jones interactions were handled via a switching function beginning at 1.0 nm, with a cutoff distance of 1.2 nm. Long-range electrostatic interactions were computed using the particle mesh ewald (PME) method, with a real-space cutoff of 1.2 nm, fourth-order B-spline interpolation, and a grid spacing chosen to achieve an accuracy of 10^{-5}. Periodic boundary conditions were applied in all three spatial dimensions, and the simulations were conducted with a time step of 2 fs.

Energy minimization was first performed on the system without water and repeated after solvation. This was followed by an *NVT* equilibration for 0.25 ns at 293.15 K using a stochastic dynamics integrator. Subsequently, an NPT equilibration of 0.5 ns was performed at 293.15 K and 1 bar, employing the Berendsen thermostat and barostat. For the final 10 ns production run in the *NPT* ensemble, the system was equilibrated at 293.15 K and 1 bar using the Nose-Hoover thermostat (relaxation time 1 ps) and the Parrinello−Rahman barostat (relaxation time 5 ps). Temperature coupling was applied independently to the water and membrane components.

3. RESULTS

3.1. Free Energy Model for Imaging Membrane Heterogeneities

To better understand the different lipid phases and to develop a framework for analyzing the small angle neutron scattering results, we first introduce a phenomenological, free-energy-based theory. Here, $\phi \equiv \phi(x, t)$ is the local fraction of one of the lipid phases (e.g., L_o or L_d) at some location, x, on the vesicle surface. Then, the free energy $\mathcal{F} \equiv \mathcal{F}[\phi]$ associated with the phase separated domains can be expanded in powers of ϕ and its gradient, $\nabla\phi$. To lowest order in the gradient, there is a line tension term proportional to $|\nabla\phi|^2$ that penalizes spatial variations of ϕ. There must also be a thermodynamic potential $V[\phi]$ that favors a phase separated state, meaning that it must have two coexisting minima at constant values $\phi = \phi_o, \phi_d$, representing the L_o and L_d phase, respectively. We must thus expand the potential $V[\phi]$ to at least quartic order in ϕ to accommodate the phase-separated state. Thus, a general form for such a free energy is given by

$$\mathcal{F}[\phi] = \int d\mathbf{x}\left[\frac{\kappa}{2}|\nabla\phi|^2 + \frac{r}{2}\phi^2 + \frac{\mu_3}{3}\phi^3 + \frac{\mu_4}{4}\phi^4\right] \quad (1)$$

where we integrate over the vesicle surface. In the above equation, r controls the distance to the phase transition as it controls the stability of the mixed phase at $\phi = 0$: A large negative r corresponds to an unstable $\phi = 0$ mixed phase, bringing us deep into the phase-separating regime where $\phi = \phi_o, \phi_d$ are favored. The coupling μ_3 sets the composition asymmetry between the two lipid phases and μ_4 sets the overall scale of the potential minima, which are given by $\phi_{o,d} = (-\mu_3 \pm \sqrt{\mu_3^2 - 4r\mu_4})/2\mu_4$. As we increase r from negative to positive values, we cross the phase transition at the critical value $r = r_c \equiv 2\mu_3^2/9\mu_4$, with $r < r_c$ corresponding to a phase-separated, ordered phase and $r > r_c$ to a "mixed" phase

https://doi.org/10.1021/acschemneuro.5c00682
ACS Chem. Neurosci. XXXX, XXX, XXX−XXX

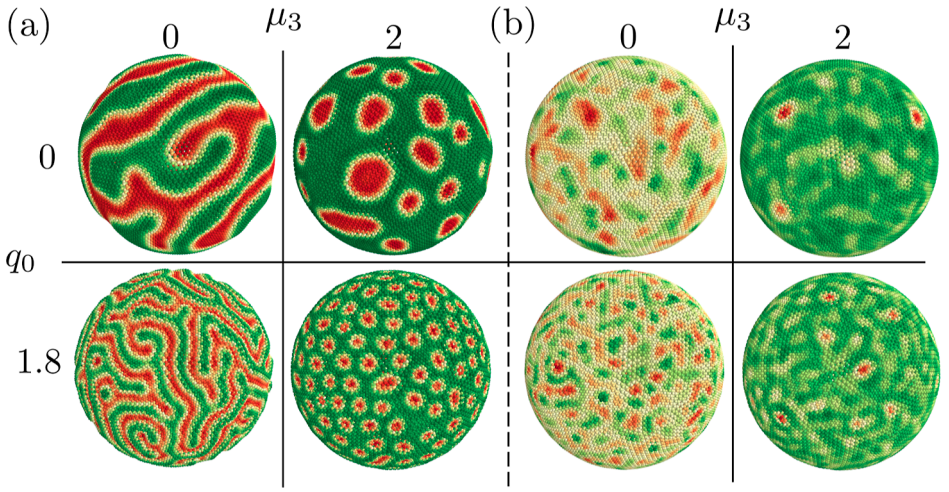

Figure 1. Numerical solutions of eq 2 showing lipid domains on a vesicle with radius, $R = 15$, where $\kappa = 0.5$, $kT = 0.2$, $\nu = 1$, and $\mu_4 = 1$ were obtained using the FiPy software package.[40] The simulation time was $t = 50$, using a random Gaussian initial condition for the field $\phi(x, t)$ with mean = 0 and a variance of 0.2. The ordered phases in (a) were evaluated at $r = -2$ and the given values of q_0 and μ_3, while the disordered phases in (b) were evaluated at $r - r_c \approx 0.6$. Note that the disordered phases still maintain some transient, domain-like structures, and it is sometimes difficult to distinguish between the various phases from a scattering experiment.

with $\phi = 0$, on average. In the absence of fluctuations, we have a second order transition for $\mu_3 = 0$, with the minima at $\phi_{o,d}$ evolving continuously away from $\phi = 0$ for $r > 0$. On the other hand, when $|\mu_3| > 0$, we have a first-order transition with metastable minima appearing whenever $r_c < r < \mu_3^2/4\mu_4$.

The line tension term is proportional to the modulus κ which sets the energy of a domain wall—a variation of ϕ from ϕ_o to ϕ_d. Note that this term may be modified if the membrane composition couples strongly to local membrane curvature,[29] resulting in a different gradient term, which is reminiscent of a "microemulsion" or a "modulated phase".[30−33] In this case, the gradient term is no longer minimized by a constant value ϕ, but rather by a spatially varying term $\phi(x)$ with some characteristic wavenumber, q_0. One then replaces $\kappa|\nabla\phi|^2$ with $\kappa\phi(\nabla^2 + q_0^2)\phi$ in eq 1. In the ordered phase, such a term will generate stripes or hexagonal arrangements of domains. These patterns are readily observed in large, micron-sized vesicles[34] and are also implicated in the surface patterning of pollen grains.[35] For nanoscopic vesicles considered here, the expected pattern size is comparable to the vesicle size and we find that our data is consistent with either $q_0 = 0$ or some small value of q_0. As a result, we opted for a simpler model where we set $q_0 = 0$. Nevertheless, we can expect a nonzero q_0 to be relevant in the description of phase-separating lipid vesicles, especially in the case of larger vesicles.

We can schematically illustrate the various phases described by eq 1 and also demonstrate the effect of noise (i.e., thermal fluctuations) by introducing dynamics to the system. We can also assume that the global fraction of the lipid phases remains fixed (as this is set by the relative abundance of the different lipid types) so that $\int dx\phi(x, t)$ remains constant as a function of time. In this case, the simplest "conserved" (model B[36]) dynamics are given by

$$\partial_t\phi(\mathbf{x}, t) = \nu\nabla^2\frac{\delta\mathcal{F}}{\delta\phi} + \eta(\mathbf{x}, t) \tag{2}$$

where $\eta(x, t)$ is a spatiotemporal noise term which satisfies, due to the fluctuation−dissipation theorem, $\langle\eta(x, t)\eta(x', t')\rangle = 2kT\nu\nabla^2\delta(x-x')\delta(t-t')$. Here, ν is a relaxation rate tending toward equilibrium, k is the Boltzmann constant, and T is the temperature. For large vesicles, such as giant unilamellar vesicles (GUVs)—most often used to construct phase diagrams and many microns in diameter[37]—the ordered phases may be readily identified using fluorescence microscopy. However, here, we consider nanoscopic vesicles for which large curvatures and small size may strongly modify their phase behavior. We also note that hydrodynamics may play an important role, especially in the motion and shape fluctuations of individual lipid domains.[38,39] We neglect these effects, as we aim to qualitatively illustrate the equilibrium distribution of lipid phases on the vesicle surface.

For the purposes of the qualitative results via numerical integration of eq 2, we set $\nu = 1$ and $kT = 0.2$, and choose a Gaussian random initial condition for $\phi(x, t = 0)$ with an average of 0 and a variance of 0.2. The other parameters are given in the Figure 1 caption. The evolution equation in eq 2 was integrated using the finite volume solver FiPy.[40] In this case, the total global fraction of the ordered phase is given by $f_0 \equiv \phi_o/(\phi_o - \phi_d)$, which can be tuned by varying μ_3, with $f_0 = 1/2$ for $\mu_3 = 0$.

The different possibilities for the ordered phases ($r(\mu_3^2/4\mu_4)$ are shown in Figure 1a for asymmetric ($\mu_3 \neq 0$) and symmetric ($\mu_3 = 0$) L_o and L_d phases. Note that it is possible to either have circular domains ($\mu_3 \neq 0$) or labyrinthine structures ($\mu_3 \approx 0$), which will coarsen until complete phase separation is achieved when $q_0 = 0$. Conversely, for modulated phases with $q_0 > 0$, we find stable ordered structures with characteristic sizes [bottom two panels in Figure 1a], which do not coarsen. Such phases also exhibit characteristic peaks in their structure factors. Note, however, that although the coarsening should continue until complete phase separation has taken place for the $q_0 = 0$ case, these dynamics may take place over a prohibitively long time, with phase separation not fully completed by the end of an experiment. This complicates the task of distinguishing between the $q_0 = 0$ and $q_0 > 0$ phases, especially for values of q_0 where $1/q_0$ is similar to the vesicle size.

Vesicles with mixed lipid phases ($r(\mu_3^2/4\mu_4)$ are shown in Figure 1b. While not technically phase separated, these phases have compositional fluctuations of length scale $\xi \approx \sqrt{\kappa/r}$,

https://doi.org/10.1021/acschemneuro.5c00682
ACS Chem. Neurosci. XXXX, XXX, XXX−XXX

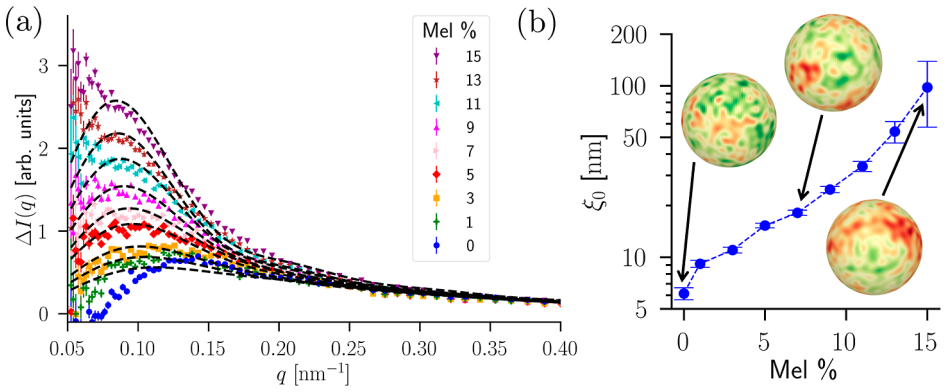

Figure 2. (a) Background-subtracted SANS intensities, $\Delta I(q)$, from $\bar{R}$ = 25 nm ULVs at T = 20 °C, demonstrating enhanced phase separation in the presence of melatonin. The black dashed lines are fits to the scattering model described in the main text, where the scattering amplitude α and the correlation length ξ are the only fitting parameters (see eq 6). The fixed parameters are the vesicle radius distribution (z = 10) and the membrane thickness (t = 4 nm). In order to take into account the scattered background from melatonin and the imperfect contrast matching, the background data from homogeneously mixed ULVs at T = 60 °C are subtracted from the domain data.[41] At 20 °C, increasing concentrations of melatonin result in larger domains—SANS peaks shift toward smaller q-values. (b) The correlation length, ξ, is determined from fits to the SANS data in part (a). Note that ξ grows dramatically with increasing melatonin concentration, indicating larger, more coherent regions of L_o and L_d phases. Some examples of possible configurations from the "ensemble" of vesicles which are consistent with the scattering results are given in the insets to the figure for corresponding melatonin concentrations.

which may appear in scattering experiments. These fluctuations become large near the phase transition and can result in the formation of transient, local L_o and L_d phases. Thus, identifying the phases of small vesicles is challenging as there may not necessarily be a sharp indicator of a transition between the mixed and phase separated states.

3.2. Lipid Phase Behavior as Revealed by Small-Angle Neutron Scattering

For SANS studies we used a dilute suspension of ULVs which were prepared by extruding a solution of multilamellar vesicles (MLVs) through a polycarbonate filter populated with 50 nm diameter pores—details are given in ref 41 In order to highlight lipid domains, we used perdeuterated DSPC (DSPC-d_{70}). At 60 °C, the lipid mixture forms a single phase whose neutron scattering length density can be matched to the buffer solution in which the ULVs reside in, thus creating a null scattering condition. While the contrast matching condition effectively reduced the scattering for $q \gtrsim 0.1$ nm^{-1}, we observed significant scattering at the smallest q values, consistent with previous studies (10, 42)—this is because one cannot achieve a perfect null scattering condition. Moreover, additional scattering was observed with increasing amounts of melatonin (see[41] for additional discussion). To isolate the scattering from lipid domains at low temperatures, we subtracted the T = 60 °C spectra from the low temperature data for each melatonin concentration. The subtracted intensities, $\Delta I(q)$, are shown in Figure 2. An additional advantage of subtracting the high temperature data, is that the incoherent scattering contribution is also minimized, simplifying the fits to the data.

The scattering intensities, $\Delta I(q)$, were modeled using a spherical harmonic expansion for the form factor. In addition, the polydispersity of the mixture was taken into account by averaging over a Schultz distribution of vesicle radii, R, given by

$$p(R) = \left[\frac{z+1}{\bar{R}}\right]^{z+1} \frac{R^z}{\Gamma(z+1)} \exp\left[-\frac{R(1+z)}{\bar{R}}\right] \quad (3)$$

where $\bar{R}$ = 25 nm is the average vesicle radius (corresponding approximately to the filter pore size) and z = 10 is a parameter which sets the standard deviation $\sigma_R = \bar{R}/\sqrt{1+z} \approx 7.5$ nm of the distribution. z = 10 was determined by an initial fit to the data and then kept fixed. Under our dilute conditions, the scattering intensity is given by the Fourier transform of the squared form factor, averaged over the distribution, $p(R)$ or as

$$\Delta I(q) = \frac{I_0}{4\pi} \int_0^\infty \int \langle |F_R(q)|^2 \rangle p(R) \mathrm{d}\Omega_{\mathbf{q}} \mathrm{d}R \quad (4)$$

where the angular brackets, $\langle \cdots \rangle$, denote a thermal average. The physics of lipid phase separation is captured by the form factor, $F_R(\mathrm{q})$, which is associated with the scattering from a single ULV of radius R—which we assume has a uniform thickness of t = 4 nm. Under neutron contrast matched conditions, the observed scattering is primarily associated with lipid heterogeneities on the vesicle surface, described by some scalar order parameter, $\psi(\theta, \phi)$ (representing the local fraction of for example, the L_o phase, and, hence, proportional to the previously mentioned field ϕ), which may be expanded into spherical harmonic modes as $\psi(\theta, \varphi) = \sum_{l,m} \psi_m^l Y_m^l(\theta, \varphi)$. These modes, then, contribute to the overall (spherically averaged) scattered intensity as follows

$$\Delta I(q) = 4\pi I_0 \sum_{l,m} \langle |\psi_m^l|^2 \rangle \times \int_0^\infty p(R) \left[\int_{R-t/2}^{R+t/2} \mathrm{d}r r^2 j_l(qr) \right]^2 \mathrm{d}R, \quad (5)$$

where $\mathrm{q} = q(\cos\theta, \cos\varphi, \cos\theta, \sin\varphi, \cos\theta)$ in spherical coordinates, $Y_m^l(\theta, \varphi)$ are the spherical harmonics, and $j_l(x)$ is the spherical Bessel function. The modes ψ_m^l depend on the lipid phase. For example, in the case of the "mixed" phase, $r > r_c$ in eq 1 will have mode magnitudes of the form

$$\langle |\psi_m^l|^2 \rangle = \frac{\alpha}{l^2 + R^2/\xi^2} \quad (6)$$

https://doi.org/10.1021/acschemneuro.5c00682
ACS Chem. Neurosci. XXXX, XXX, XXX−XXX

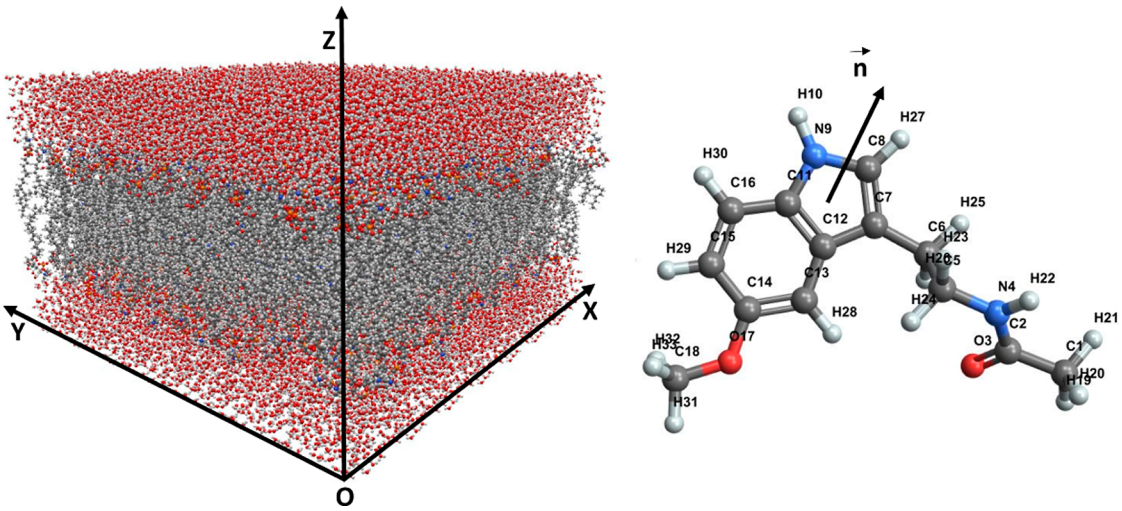

Figure 3. Left: atomistic representation of a fully hydrated lipid bilayer. Water molecules are shown in red and white, forming a solvation shell above and below the membrane. Lipid molecules are rendered in gray with embedded melatonin molecules present, which are not explicitly highlighted. The different axis (x, y, z) denote the simulation box coordinates, with the z-axis aligned normal to the membrane plane. Right: Molecular structure of melatonin showing labeled atoms (carbon (gray), hydrogen (white), nitrogen (blue), and oxygen (red)). Functional groups include the indole ring, the methoxy group (CH_3O), and the acetamide moiety (CH_3CONH). The black arrow indicates a unit vector $\vec{n}$ normal to the indole ring plane which is used to define the molecular tilt angle θ relative to the membrane normal (z-axis).

where ξ is the correlation length and α is a constant amplitude. In this simple model, ξ gives us some idea of domain size, but does not give us a full picture of the domain morphology. However, the model has the advantage of having just two fitting parameters: the correlation length, ξ, and the amplitude, α, which can be integrated into the overall amplitude I_0 in eq 5. All other terms in eq 5 can be determined independently and are constant across all melatonin concentrations studied here. The lipid bilayer thickness was taken to be t = 4 nm and the average vesicle radius, $\overline{R}$ = 25 nm. These values along with the polydispersity parameter z = 10 completely describe the distribution, $p(R)$, given in eq 3. Any other contributions, such as incoherent scattering and scattering from imperfect contrast matching is removed by background subtraction. The resultant scattering profile $\Delta I(q)$ can thus be fit using just ξ and α. The results are shown in Figure 2a.

Variation in domain morphology due to increasing melatonin concentration can be captured by ξ. The amplitudes α in eq 6 vary by about a factor of 2, while ξ varies by more than an order of magnitude, as shown in Figure 2b. These indicate a significant change in domain structure namely, at low melatonin concentrations the structures predominantly consist of spherical harmonic modes in the range $l \approx 5$, corresponding to multiple L_o and L_d domains populating ULVs. Conversely, at the largest melatonin concentration (15 mol %), the contributions to scattering are due to harmonic modes near l = 1. At this melatonin concentration (15 mol %), we expect the vesicle to be completely phase separated. Some example structures are shown in the insets to Figure 2b. Note that the SANS scattering results inform us about the size of domains, but cannot capture details at smaller length scales, such as the precise shapes of the domain boundaries, which could be as disordered as the domains (Figure 1b), or not (Figure 1a). The general conclusion is that as melatonin concentration increases, the overall size of the "coherent" structures (local regions of L_o and L_d phases as captured by ξ) also increases. These increases, as seen in Figure 2b, tend to be largest for melatonin concentrations less than 5% and greater than 10%, with the intermediate concentrations between 5% and 10% showing a slightly more modest increase in ξ.

3.3. Molecular Insights from All-Atom Molecular Dynamics Simulations

For the most part, melatonin adopts two orientations in aqueous solution, both of which are dictated by its amphiphilic nature and the polarity of its functional groups. The spatial arrangement of its indole ring, methoxy group ($-OCH_3$), and acetamide moiety ($-CONH_2$) governs the balance between hydrogen bonding and hydrophobic interactions with its surrounding water.[42] In its energetically preferred conformation, melatonin orients its polar acetamide group which contains both a hydrogen bond donor ($-NH$) and acceptor ($C{=}O$), thereby maximizing directional hydrogen bonding while shielding its hydrophobic indole core.[42] This spatial configuration stabilizes melatonin's solvation shell, enhances its aqueous solubility, and facilitates its migration across membrane environments. Consistent with MD simulations and prior structural modeling studies, this conformation promotes interaction with cytosolic water molecules and influences melatonin's intracellular distribution and capacity to modulate cytoskeletal structures, such as microtubules.[43] A secondary, less favorable orientation transiently exposes its methoxy group and part of its indole ring to the solvent. Although the methoxy oxygen can participate in weak hydrogen bonding, the increased solvent exposure of the aromatic ring renders this conformation less stable. Nevertheless, thermal fluctuations permit the coexistence of both states, highlighting melatonin's structural adaptability to diverse microenvironments.[44]

To investigate this behavior in a biologically relevant context, we performed all-atom MD simulations on a fully hydrated, phase-separated neuronal membrane model. Figure 3 (left) shows a simulation snapshot of melatonin embedded in the lipid bilayer, surrounded by explicit water (red and white spheres). The right panel depicts the molecular structure of melatonin with annotated atoms and a unit vector $\vec{n}$

https://doi.org/10.1021/acschemneuro.5c00682
ACS Chem. Neurosci. XXXX, XXX, XXX−XXX

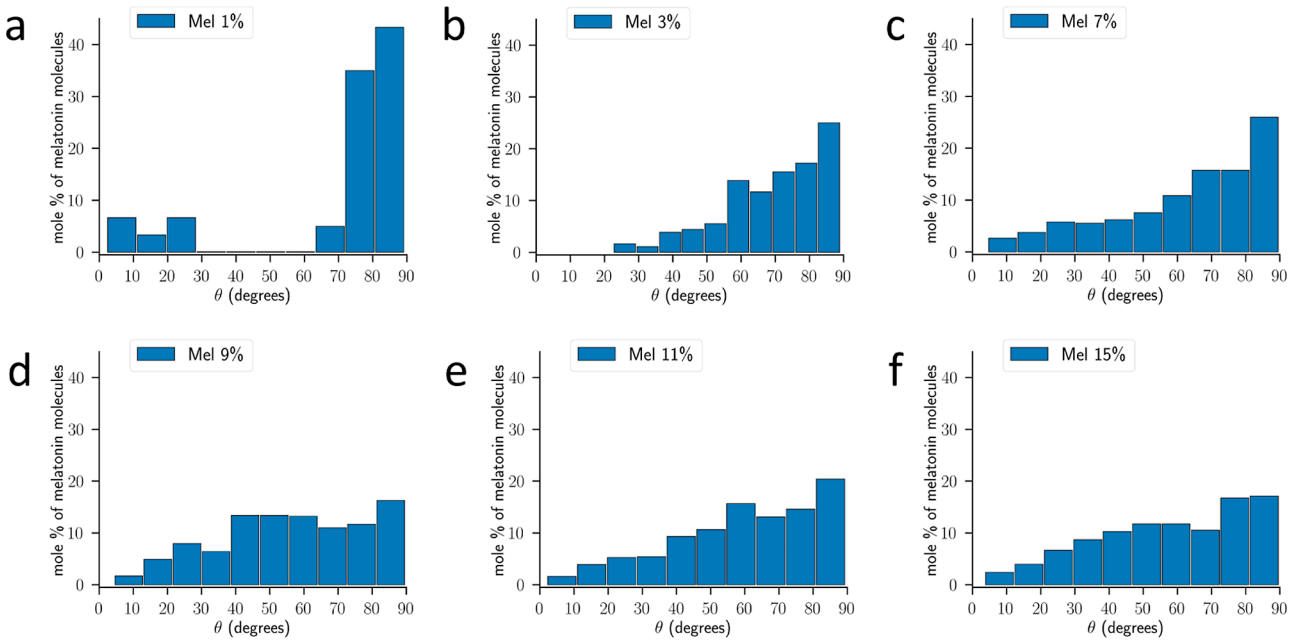

Figure 4. Tilt angle distribution, θ, between the membrane normal (z axis, see Figure 3) and the unit vector, $\vec{n}$, normal to melatonin's indole ring, computed at various melatonin molar concentrations. The histograms illustrate the mole percentage of melatonin molecules adopting specific orientation angles within the lipid bilayer for 1%, 3%, 7%, 9%, 11%, and 15% melatonin. A shift toward broader and more uniform angular distributions is observed with increasing melatonin concentration, indicating enhanced orientational disorder and the emergence of diverse alignment states within the bilayer interior.

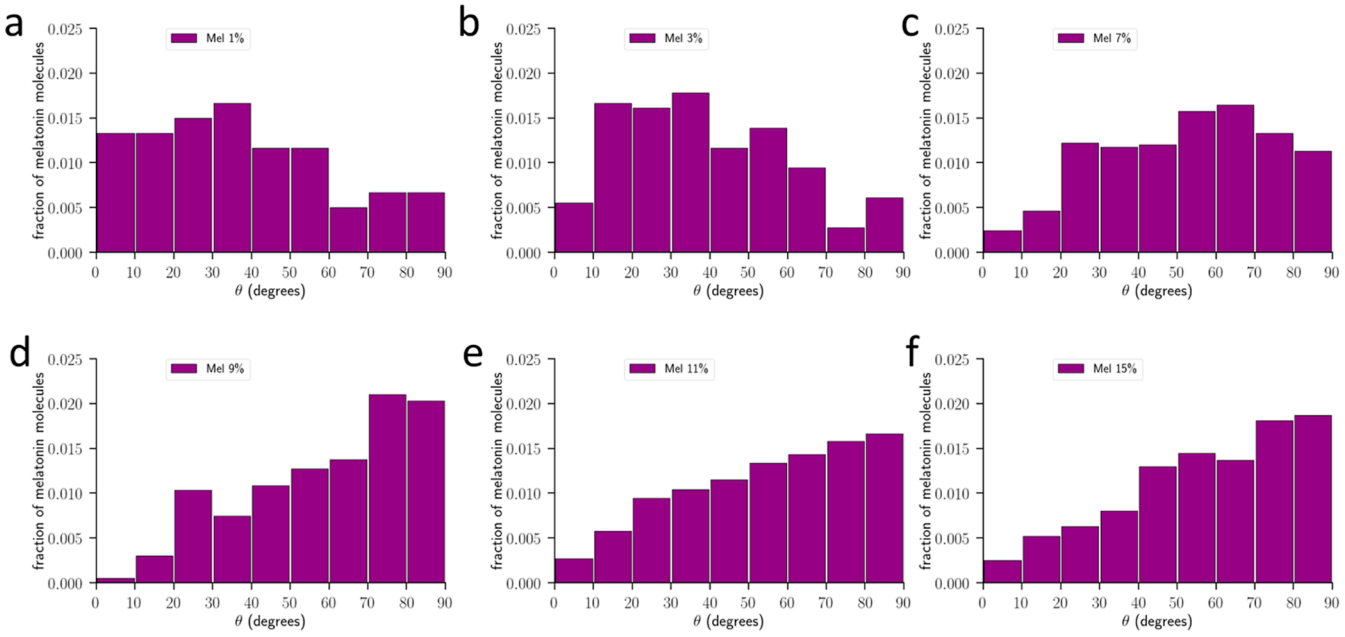

Figure 5. Tilt angle distribution, θ, between the membrane normal (z axis, see Figure 3) and the C−O bond vector within melatonin's carboxyl functional group, calculated at different melatonin molar concentrations. Each histogram represents the mole percentage of melatonin molecules exhibiting a given tilt angle for 1%, 3%, 7%, 9%, 11%, and 15% melatonin amounts. The data reveal a progressive broadening of the angular distribution and increased tilt heterogeneity with higher melatonin content, suggesting more dynamic orientational states within the lipid bilayer interface.

perpendicular to the indole plane which is used in subsequent analyses.

Figure 4 presents the angular distribution of melatonin molecules relative to the membrane normal characterized by the tilt angle, θ, between the z axis (normal to the bilayer plane) and the unit vector, $\vec{n}$, normal to melatonin's indole ring. The histograms, shown for six different melatonin molar fractions (1%, 3%, 7%, 9%, 11%, and 15%), quantify the mole percentage of melatonin molecules in a given orientation. At low concentrations (1−3%), the distributions are sharply peaked near θ = 80°−90°, indicating a strong preference for the indole ring normal $\vec{n}$ to align roughly perpendicular to the bilayer plane normal, consistent with interfacial localization at the headgroup−water interface.[45] As the melatonin content

https://doi.org/10.1021/acschemneuro.5c00682
ACS Chem. Neurosci. XXXX, XXX, XXX−XXX

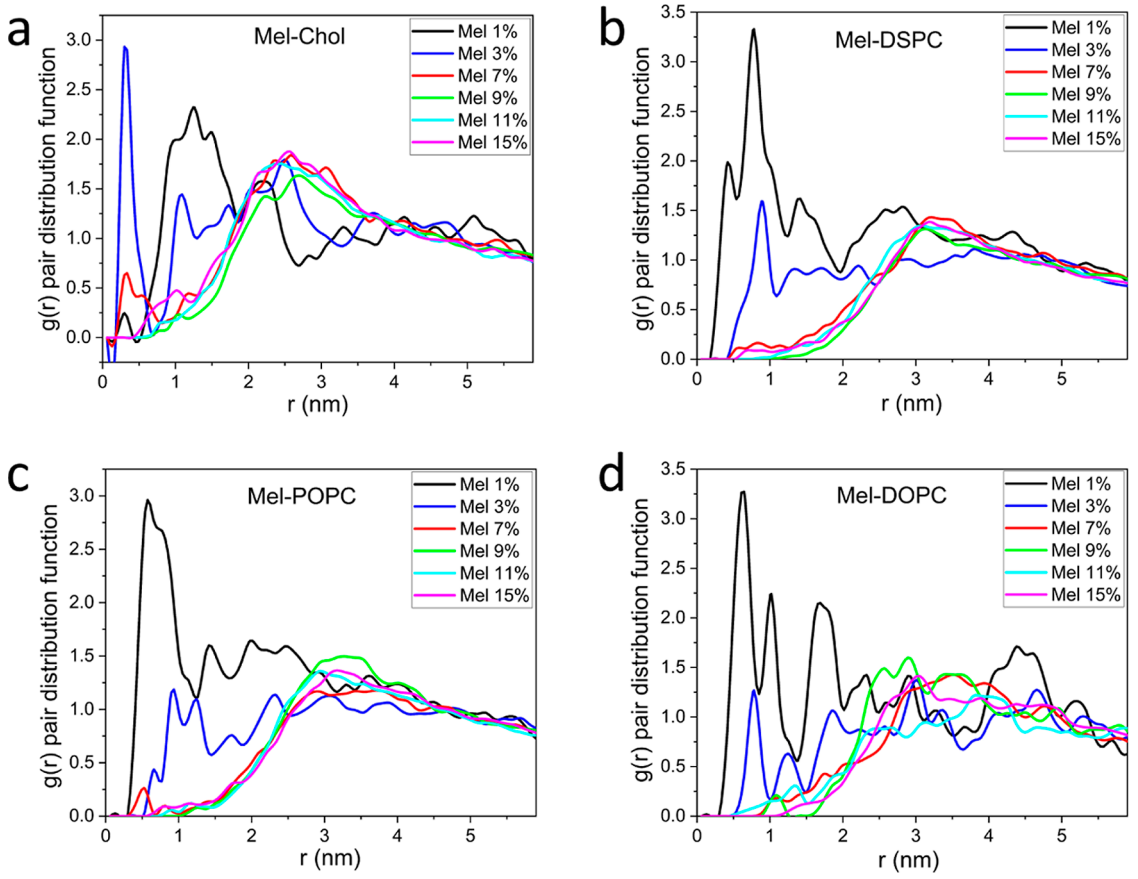

Figure 6. Pair distribution functions (PDFs), $g(r)$, computed from all-atom MD simulations of a fully hydrated, phase-separated lipid bilayer system containing different amounts of melatonin (Mel). Center-of-mass correlations are shown between melatonin and (a) cholesterol (Chol), (b) distearoylphosphatidylcholine (DSPC), (c) palmitoyloleoylphosphatidylcholine (POPC), and (d) dioleoylphosphatidylcholine (DOPC). Each curve corresponds to a different melatonin molar ratio: 1%, 3%, 7%, 9%, 11%, and 15%. These plots reveal the spatial organization and interaction strength of melatonin with each lipid component as a function of radial distance, r, in nanometers. Notably, the first peak in $g(r)$ reflects the preferred separation distances and coordination environment between melatonin and the respective lipid species.

increases, the distributions progressively broaden and shift, with an increasing population of molecules adopting intermediate orientations. This behavior suggests that higher melatonin loading introduces greater orientational disorder and promotes deeper membrane insertion or lateral packing constraints, thereby reducing the rigidity of the preferred interfacial alignment.

In contrast, Figure 5 reports the tilt angle distributions of the C− O bond within melatonin's carboxyl functional group relative to the same membrane normal. Across all concentrations, the distributions are broader than those observed for the indole ring and their modal angles are systematically lower. Notably, as melatonin concentration increases, the C−O bond orientations shift continuously toward lower tilt angles (i.e., closer to alignment with the membrane normal). This is particularly evident at 9−15% melatonin. These results indicate that the carboxyl group—which is more hydrophilic than the indole moiety—remains more conformationally dynamic and may engage more directly with the aqueous phase or the polar headgroups. The smoother and more gradual evolution of these distributions across concentrations highlights the structural flexibility of the C− O bond and its sensitivity to local membrane hydration and packing.

A comparison between the two figures shows that various regions of the melatonin molecule adopt different orientations and adjust their positioning based on its concentration. While the indole ring maintains a strong interfacial orientation at low melatonin fractions, and only gradually loses its order at higher loading, the carboxyl group remains more dynamically responsive and less constrained throughout the concentration range. These results underscore the dual role of melatonin as both an interfacial and partially embedded molecule within the membrane, with its amphipathic nature allowing different segments to interact differentially between the lipid and aqueous environments. Collectively, this orientational behavior supports a model in which melatonin bridges the lipid headgroups with the bulk water, thus modulating membrane order and hydration in a concentration-dependent manner. Notably, the observed interleaflet bridging configurations may facilitate signal transduction across the bilayer, enabling communication from the extracellular to the cytoplasmic environment through a receptor-independent mechanism.[46]

To quantify structural correlations between melatonin and membrane components, the pair distribution function (PDF), or radial distribution function, $g(r)$, is employed. This function measures the probability density of finding a particle A at a distance r from a reference particle B—normalized by the expectation for an ideal gas at the same average number density.[47,48] For a binary system with N_A and N_B particles and simulation volume, V, the cross-correlation PDF is given by

https://doi.org/10.1021/acschemneuro.5c00682
ACS Chem. Neurosci. XXXX, XXX, XXX−XXX

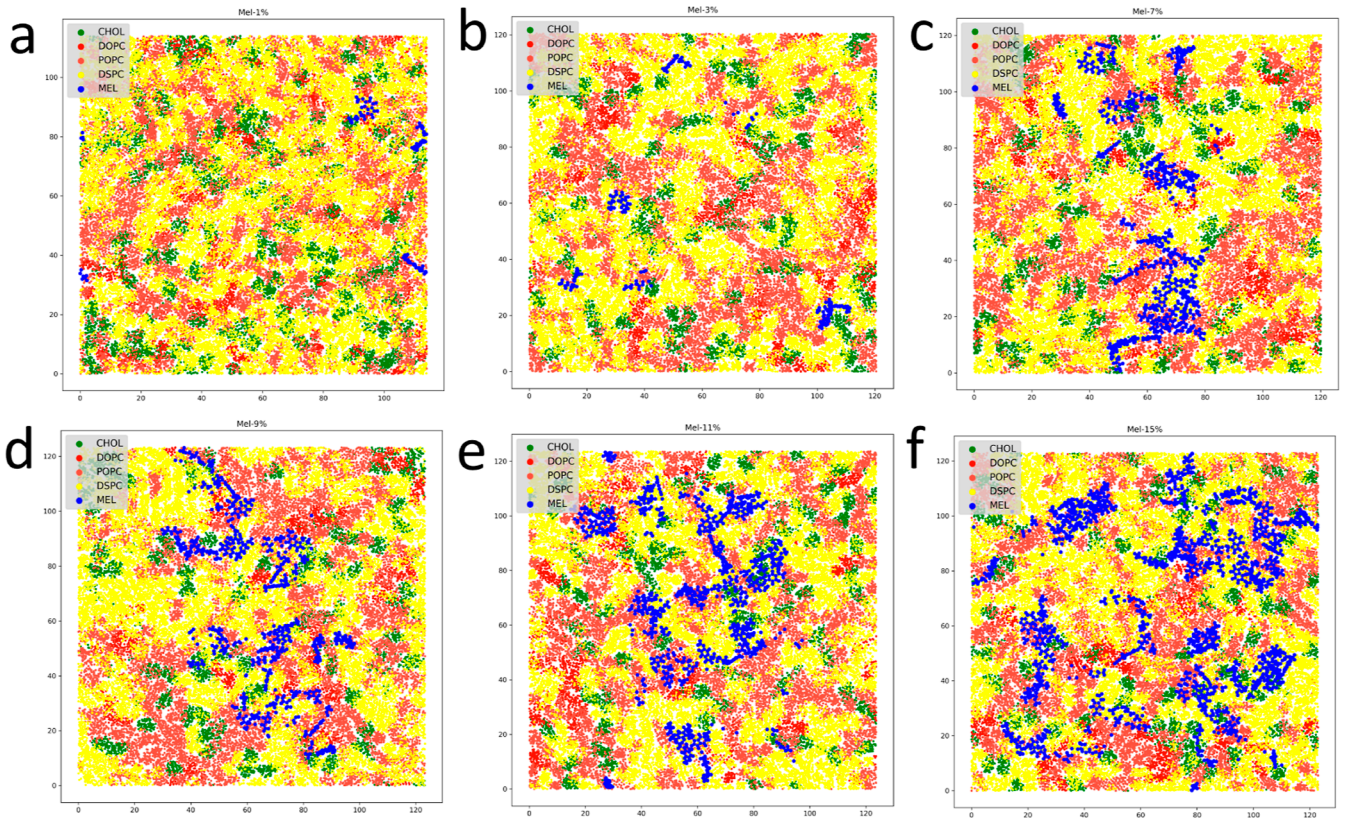

Figure 7. Spatial distributions of the centers of mass of lipid headgroups in ternary phase-separated bilayers composed of saturated DSPC (yellow), unsaturated POPC (red), diunsaturated DOPC (orange), cholesterol (green), and melatonin (blue), shown as a function of increasing melatonin concentrations. Snapshots are derived from all-atom MD simulations and reveal robust liquid−liquid phase separation with the formation of distinct microdomains. Cholesterol and melatonin preferentially accumulate near domain interfaces, contributing to local structural organization. At higher melatonin levels, the emergence of short-range, honeycomb-like ordering is observed within melatonin-rich regions, suggesting nanoscale structuring and interdomain bridging driven by melatonin.

$$g(r) = \frac{V}{4\pi r^2 N_A N_B} \left\langle \sum_{i=1}^{N_A} \sum_{j=1}^{N_B} \delta(r - |r_{Ai} - r_{Bj}|) \right\rangle \quad (7)$$

where $|r_{Ai}-r_{Bj}|$ is the distance between the ith particle of type A and the jth particle of type B, and $\langle\cdot\rangle$ is the ensemble average over time or configurations. The $4\pi r^2$ in the prefactor in front of the average accounts for the surface area of a spherical shell at distance r, ensuring proper normalization. This approach enables quantitative evaluation of radial proximity and coordination tendencies between melatonin and specific lipid species in the membrane, providing a structural framework to interpret solute−lipid interaction strength and local organization.

Figure 6 presents the pair distribution functions, $g(r)$, computed between the center of mass of melatonin and the four membrane lipids: cholesterol (a), DSPC (b), POPC (c), and DOPC (d), across a series of melatonin concentrations (1% to 15% molar ratio). These curves quantify the spatial probability of locating each lipid type at a given distance from melatonin, offering insight into local coordination environments and preferential interactions.

At low melatonin concentrations (1−3%), PDFs display sharp, well-defined peaks, particularly for melatonin—cholesterol and melatonin−DSPC distributions (panels a and b, respectively), suggesting strong spatial ordering and preferential interactions with saturated and sterol-rich domains. In contrast, at elevated melatonin concentrations (7−15%), the peaks broaden and decrease in intensity, indicating a progressive loss of structural specificity and dilution of preferential lipid associations. In lipids with unsaturated fatty acids chains (POPC and DOPC, panels c and d), melatonin exhibits broader, less structured distributions across all concentrations, consistent with reduced packing constraints in L_d regions. Notably, the first coordination shell for melatonin—cholesterol interactions remains distinct up to moderate concentrations, underscoring cholesterol's role as a dominant binding partner and potential mediator of melatonin partitioning into L_o domains. These findings support a model in which melatonin initially targets ordered lipid environments, but with increasing concentration, diffuses more broadly across both L_o and L_d phases, modulating bilayer organization and heterogeneity in a dose-dependent manner.

To visualize the spatial partitioning behavior of melatonin across phase-separated lipid bilayers, we analyzed the lateral distributions of lipid headgroup centers of mass at multiple melatonin concentrations. This analysis also highlights the role of dipolar orientations in phospholipid membranes, which modulate surface undulations, coupled with polar water, and facilitate lateral and transmembrane heat transfer and energy transduction.[49] These processes may be influenced by melatonin's positioning and orientation within the bilayer. The snapshots reveal the progressive reorganization of membrane architecture as melatonin is incorporated into the system, see Figure 7. At low concentrations, melatonin is sparsely distributed near domain interfaces. However, as its

https://doi.org/10.1021/acschemneuro.5c00682
ACS Chem. Neurosci. XXXX, XXX, XXX−XXX

concentration increases, it aggregates into interconnected patterns that span multiple lipid environments. This lateral redistribution coincides with enhanced melatonin mixing at domain boundaries and partial remodeling of L_o and L_d domains. Although DSPC-rich regions retain their structural integrity, POPC and DOPC regions exhibit more diffuse boundaries. Cholesterol concentrates at interfacial boundaries and colocalizes with melatonin in several instances, suggesting cooperative interactions. Notably, melatonin-rich clusters become more spatially ordered and interconnected at higher concentrations, forming motifs consistent with nanoscale patterning and domain bridging behavior. These observations highlight melatonin's capacity to modulate lateral heterogeneity within complex lipid mixtures and suggest its potential role in stabilizing or remodeling lipid nanodomains relevant to neuronal membrane dynamics.

4. DISCUSSION AND CONCLUSIONS

Our findings demonstrate that melatonin exerts a profound influence on the structural organization of cholesterol-rich neuronal membrane mimics. By combining SANS and all-atom MD simulations, the data reveal a multiscale mechanism by which melatonin stabilizes, modulates, and bridges lipid microdomains in a concentration-dependent manner.

At the mesoscopic scale, SANS data provide compelling evidence that melatonin promotes the formation and growth of phase-separated domains in unilamellar vesicles. The emergence of well-defined scattering features at low scattering vectors and the increase in the correlation length, ξ, with increasing amounts of melatonin, indicate that melatonin drives the system toward enhanced nanodomain coherence. This structural reorganization suggests that melatonin facilitates line tension modulation and interfacial stabilization between the L_o and L_d phases. Notably, we observe this behavior at physiologically relevant concentrations (<15 mol %), reinforcing the potential biological relevance of these findings. Interestingly, seratonin, a melatonin precursor with an opposite physiological effect has been shown to, on the contrary, destabilize ordered domains in model membranes.[50]

Complementary MD simulations elucidate the molecular underpinnings of this behavior. PDF analyses reveal that melatonin preferentially localizes near cholesterol and saturated lipid species (e.g., DSPC), particularly at lower concentrations. These findings highlight the intrinsic affinity of melatonin for L_o-like regions, where tight lipid packing and cholesterol content are greatest. However, with increasing concentration, melatonin distributes itself across both L_o and L_d phases, reflecting a shift from selective interfacial localization to broader bilayer interactions. This transition is accompanied by increased orientational disorder of melatonin's indole and carboxyl groups, suggesting the molecule inserting itself deeper in the bilayer's hydrophobic core, possibly disrupting lipid acyl chain packing.

Spatial distribution maps further support this interpretation, showing that melatonin accumulates near domain boundaries at low concentration, but forms extended, honeycomb-like networks as melatonin concentration increases. These lateral aggregates are suggestive of short-range positional order and interfacial bridging behavior, with melatonin acting as a molecular scaffold stabilizing domain morphology. Such domain bridging could have far-reaching consequences for the spatial organization of membrane proteins and signal transduction platforms in neuronal membranes.[51]

From a biological standpoint, these findings expand our understanding of how small, amphiphilic molecules, like melatonin, may modulate membrane biophysics independently of receptor-mediated pathways. Neuronal membranes are not inert dielectric sheets but responsive,[52] compositionally complex materials capable of memory-like behavior through structural plasticity.[53,54] By stabilizing phase-separated domains and modulating lipid packing, melatonin may influence protein sorting, receptor clustering, and signal propagation within the synaptic environment. Moreover, the ability to reshape membrane architecture in a concentration-dependent fashion suggests that melatonin could serve as a dynamic regulator of membrane heterogeneity under physiological or pathological conditions.[55]

Finally, this work lays the groundwork for exploring melatonin's role in neuroprotection from a membrane-centric perspective. Altered lipid raft dynamics and cholesterol dysregulation are hallmarks of neurodegenerative diseases, including Alzheimer's and Parkinson's. Melatonin's capacity to interact with cholesterol-rich domains, reorganize nanoscale order, and bridge functional membrane regions suggests a new biophysical pathway by which it may support neuronal resilience. This idea has also recently been explored with seratonin, a similar small molecule which can modify the lipid membrane organization and with demonstrated, nonspecific allosteric functionality on membrane receptors.[6]

In conclusion, melatonin emerges as a biophysically active modulator of membrane heterogeneity, capable of tuning domain morphology, lipid organization, and interfacial connectivity. This membrane-centric mechanism complements its classical receptor-driven actions and opens new avenues for therapeutic strategies targeting the structural underpinnings of neuronal signaling and stability.

AUTHOR INFORMATION

Corresponding Authors

Dima Bolmatov − *Department of Physics and Astronomy, Texas Tech University, Lubbock, Texas 79409, United States; Shull-Wollan Center, Oak Ridge National Laboratory, Oak Ridge, Tennessee 37831, United States;* orcid.org/0000-0003-4179-8971; Email: dima.bolmatov@ttu.edu

Maxim O. Lavrentovich − *Department of Earth, Environment, and Physics, Worcester State University, Worcester, Massachusetts 01602, United States; Department of Physics and Astronomy, University of Tennessee, Knoxville, Tennessee 37996, United States;* orcid.org/0000-0002-5125-7979; Email: lavrentm@gmail.com

Authors

Russel J. Reiter − *Department of Cell Systems and Anatomy, UT Health, Long School of Medicine, San Antonio, Texas 78229, United States*

Dmitry Zav'yalov − *Volgograd State Technical University, Volgograd 400005, Russia*

Changwoo Do − *Volgograd State Technical University, Volgograd 400005, Russia;* orcid.org/0000-0001-8358-8417

Gergely Nagy − *Neutron Scattering Division, Oak Ridge National Laboratory, Oak Ridge, Tennessee 37831, United States;* orcid.org/0000-0003-2742-0198

Charles Patrick Collier − *Center for Nanophase Materials Sciences, Oak Ridge National Laboratory, Oak Ridge,*

https://doi.org/10.1021/acschemneuro.5c00682
ACS Chem. Neurosci. XXXX, XXX, XXX−XXX

Tennessee 37831, United States; orcid.org/0000-0002-8198-793X

John Katsaras − *Neutron Scattering Division, Oak Ridge National Laboratory, Oak Ridge, Tennessee 37831, United States; Shull-Wollan Center, Oak Ridge National Laboratory, Oak Ridge, Tennessee 37831, United States;* orcid.org/0000-0002-8937-4177

Complete contact information is available at: https://pubs.acs.org/10.1021/acschemneuro.5c00682

Author Contributions

D.B., M.O.L.: investigation; formal analysis; methodology; validation; data acquisition and interpretation; visualization; writing—original draft; funding acquisition. D.Z.: computer modeling; data analysis. R.J.R., C.P.C., J.K.: writing—review and editing. C.D., G.N.: neutron scattering; data acquisition.

Notes

The authors declare no competing financial interest.

■ ACKNOWLEDGMENTS

D.B. and M.O.L. are supported by the National Science Foundation, Division of Molecular and Cellular Biosciences (MCB), under award number 2219289. J.K. and C.P.C. are supported by the Scientific User Facilities Division of the U.S. Department of Energy (DOE), Office of Basic Energy Sciences (BES), under contract number DE-AC05-00OR2275 and partially supported by the Nonequilibrium and Emergent Transients in Advanced and Soft Materials (NEAT), Laboratory Directed Research and Development Program of Oak Ridge National Laboratory, managed by UT-Battelle, LLC, for the US DOE. A portion of this research used resources at the Spallation Neutron Source, as appropriate, a DOE Office of Science User Facility operated by the Oak Ridge National Laboratory. The beam time was allocated to EQ-SANS (BL-6) on proposal number IPTS-25214. Portions of the computational work were performed at the Center for Nanophase Materials Sciences (CNMS), a DOE Office of Science User Facility at Oak Ridge National Laboratory.

■ REFERENCES

(1) Reiter, R. J.; Tan, D.-X.; Manchester, L. C.; Qi, W. *Progress in Brain Research*; Elsevier, 2001; Vol. *122*, pp 359−365.

(2) Tan, D.-X.; Manchester, L. C.; Terron, M. P.; Flores, L. J.; Reiter, R. J. One molecule, many derivatives: A never-ending interaction of melatonin with reactive oxygen and nitrogen species? *J. Pineal Res.* **2007**, *42*, 28−42.

(3) Reiter, R. J.; Sharma, R. N.; Manucha, W.; Rosales-Corral, S.; de Almeida Chuffa, L. G.; Loh, D.; Luchetti, F.; Balduini, W.; Govitrapong, P. Dysfunctional mitochondria in age-related neurodegeneration: Utility of melatonin as an antioxidant treatment. *Ageing Res. Rev.* **2024**, *101*, 102480.

(4) Wei, J.; Liu, H.; Li, Y.; Zhao, D.; Wang, B.; Wang, H.; Wang, L.; Wang, K.; Yue, J.; Zhang, H.; et al. Melatonin protects against cocaine-induced blood-brain barrier dysfunction and cognitive impairment by regulating miR-320a-dependent GLUT1 expression. *J. Pineal Res.* **2024**, *76*, No. e70002.

(5) Peters, G. H.; Wang, C.; Cruys-Bagger, N.; Velardez, G. F.; Madsen, J. J.; Westh, P. Binding of serotonin to lipid membranes. *J. Am. Chem. Soc.* **2013**, *135*, 2164−2171.

(6) Roy, D. S.; Gozzi, M.; Engberg, O.; Adler, J.; Huster, D.; Maiti, S. Membrane-mediated allosteric action of serotonin on a noncognate G-protein-coupled receptor. *J. Phys. Chem. Lett.* **2024**, *15*, 1711−1718.

(7) O'Brien, J. S.; Sampson, E. L. Lipid composition of the normal human brain: gray matter, white matter, and myelin. *J. Lipid Res.* **1965**, *6*, 537−544.

(8) Sastry, P. S. Lipids of nervous tissue: composition and metabolism. *Prog. Lipid Res.* **1985**, *24*, 69−176.

(9) Heberle, F. A.; Petruzielo, R. S.; Pan, J.; Drazba, P.; Kučerka, N.; Standaert, R. F.; Feigenson, G. W.; Katsaras, J. Bilayer thickness mismatch controls domain size in model membranes. *J. Am. Chem. Soc.* **2013**, *135*, 6853−6859.

(10) Nickels, J. D.; Chatterjee, S.; Stanley, C. B.; Qian, S.; Cheng, X.; Myles, D. A.; Standaert, R. F.; Elkins, J. G.; Katsaras, J. The in vivo structure of biological membranes and evidence for lipid domains. *PLoS Biol.* **2017**, *15*, No. e2002214.

(11) Nickels, J. D.; Cheng, X.; Mostofian, B.; Stanley, C.; Lindner, B.; Heberle, F. A.; Perticaroli, S.; Feygenson, M.; Egami, T.; Standaert, R. F.; Smith, J. C.; Myles, D. A. A.; Ohl, M.; Katsaras, J. Mechanical properties of nanoscopic lipid domains. *J. Am. Chem. Soc.* **2015**, *137*, 15772−15780.

(12) Saher, G.; Stumpf, S. K. Cholesterol in myelin biogenesis and hypomyelinating disorders. *Biochim. Biophys. Acta Mol. Cell Biol. Lipids* **2015**, *1851*, 1083−1094.

(13) Kister, A.; Kister, I. Overview of myelin, major myelin lipids, and myelin-associated proteins. *Front. Chem.* **2023**, *10*, 1041961.

(14) Fantini, J.; Yahi, N. *Brain Lipids in Synaptic Function and Neurological Disease: Clues to Innovative Therapeutic Strategies for Brain Disorders*; Academic Press, 2015.

(15) Kato, D.; et al. Regulation of lipid synthesis in myelin modulates neural activity and is required for motor learning. *Glia* **2023**, *71*, 2591−2608.

(16) Bolmatov, D.; Lavrentovich, M.; Reiter, R. J. Molecular interactions of melatonin with lipid rafts. *Melatonin Research* **2022**, *5*, 101−113.

(17) Bolmatov, D.; Soloviov, D.; Zhernenkov, M.; Zav'yalov, D.; Mamontov, E.; Suvorov, A.; Cai, Y. Q.; Katsaras, J. Molecular picture of the transient nature of lipid rafts. *Langmuir* **2020**, *36*, 4887−4896.

(18) Kleszczynski, K.; Fischer, T. W. Melatonin and the Skin: Amphiphilic Actions of Melatonin in Membranes. *Int. J. Mol. Sci.* **2022**, *23*, 103.

(19) Jang, H.; Min, H. K.; Nam, J. H. Melatonin-induced membrane phase separation in model lipid rafts: Implications for signaling modulation. *Biochim. Biophys. Acta Biomembr.* **2023**, *1866*, 184222.

(20) Gupta, A.; Krupa, P.; Engberg, O.; Krupa, M.; Chaudhary, A.; Li, M. S.; Huster, D.; Maiti, S. Unusual robustness of neurotransmitter vesicle membranes against serotinin-induced perturbations. *J. Phys. Chem. B* **2023**, *127*, 1947−1955.

(21) Zhao, J. K.; Gao, C. Y.; Liu, D. The extended *Q*-range small-angle neutron scattering diffractometer at the SNS. *J. Appl. Crystallogr.* **2010**, *43*, 1068−1077.

(22) Heller, W. T.; Cuneo, M.; Debeer-Schmitt, L.; Do, C.; He, L.; Heroux, L.; Littrell, K.; Pingali, S. V.; Qian, S.; Stanley, C.; Urban, V. S.; Wu, B.; Bras, W. The suite of small-angle neutron scattering instruments at Oak Ridge National Laboratory. *J. Appl. Crystallogr.* **2018**, *51*, 242−248.

(23) Arnold, O.; et al. Mantid−Data analysis and visualization package for neutron scattering and μ SR experiments. *Nucl. Instrum. Methods Phys. Res. A* **2014**, *764*, 156−166.

(24) Heller, W. T.; et al. drtsans: The data reduction toolkit for small-angle neutron scattering at Oak Ridge National Laboratory. *SoftwareX* **2022**, *19*, 101101.

(25) Jo, S.; Kim, T.; Iyer, V. G.; Im, W. CHARMM-GUI: a web-based graphical user interface for CHARMM. *J. Comput. Chem.* **2008**, *29*, 1859−1865.

(26) Lee, J.; et al. CHARMM-GUI membrane builder for complex biological membrane simulations with glycolipids and lipoglycans. *J. Chem. Theory Comput.* **2019**, *15*, 775−786.

(27) Hess, B.; Kutzner, C.; Van Der Spoel, D.; Lindahl, E. GROMACS 4: algorithms for highly efficient, load-balanced, and scalable molecular simulation. *J. Chem. Theory Comput.* **2008**, *4*, 435−447.

(28) Huang, J.; Rauscher, S.; Nawrocki, G.; Ran, T.; Feig, M.; De Groot, B. L.; Grubmüller, H.; MacKerell, A. D. CHARMM36m: an improved force field for folded and intrinsically disordered proteins. *Nat. Methods* **2017**, *14*, 71−73.
(29) Leibler, S.; Andelman, D. Ordered and curved meso-structures in membranes and amphiphilic films. *J. Phys. (Paris)* **1987**, *48*, 2013−2018.
(30) Konyakhina, T. M.; Goh, S. L.; Amazon, J.; Heberle, F. A.; Wu, J.; Feigenson, G. W. Control of a Nanoscopic-to-Macroscopic Transition: Modulated Phases in Four-Component DSPC/DOPC/POPC/Chol Giant Unilamellar Vesicles. *Biophys. J.* **2011**, *101*, L8−L10.
(31) Lavrentovich, M. O.; Horsley, E. M.; Radja, A.; Sweeney, A. M.; Kamien, R. D. First-order patterning transitions on a sphere as a router to cell morphology. *Proc. Natl. Acad. Sci.* **2016**, *113*, 5189−5194.
(32) Schick, M. Membrane heterogeneity: Manifestation of a curvature-induced microemulsion. *Phys. Rev. E:Stat., Nonlinear, Soft Matter Phys.* **2012**, *85*, 031902.
(33) Shlomovitz, R.; Maibaum, L.; Schick, M. Macroscopic Phase Separation, Modulated Phases, and Microemulsions: A Unified Picture of Rafts. *Biophys. J.* **2014**, *106*, 1979−1985.
(34) Baumgart, T.; Hess, S. T.; Webb, W. W. Imaging coexisting fluid domains in biomembrane models coupling curvature and line tension. *Nature* **2003**, *425*, 821−824.
(35) Radja, A.; Horsley, E. M.; Lavrentovich, M. O.; Sweeney, A. M. Pollen cell wall patterns form from modulated phases. *Cell* **2019**, *176*, 856−868.
(36) Hohenberg, P. C.; Halperin, B. I. Theory of dynamic critical phenomena. *Rev. Mod. Phys.* **1977**, *49*, 435.
(37) Goñi, F. M.; Alonso, A.; Bagatolli, L. A.; Brown, R. E.; Marsh, D.; Prieto, M.; Thewalt, J. L. Phase diagrams of lipid mixtures relevant to the study of membrane rafts. *Biochim. Biophys. Acta Gen. Subj.* **2008**, *1781*, 665−684.
(38) Camley, B. A.; Brown, F. L. H. Dynamic Simulations of Multicomponent Lipid Membranes over Long Length and Time Scales. *Phys. Rev. Lett.* **2010**, *105*, 148102.
(39) Brown, F. L. H. Continuum simulations of biomembrane dynamics and the importance of hydrodynamic effects. *Q. Rev. Biophys.* **2011**, *44*, 391−432.
(40) Guyer, J. E.; Wheeler, D.; Warren, J. A. FiPy: Partial Differential Equations with Python. *Comput. Sci. Eng.* **2009**, *11*, 6−15.
(41) Bolmatov, D.; McClintic, W. T.; Taylor, G.; Stanley, C. B.; Do, C.; Collier, C. P.; Leonenko, Z.; Lavrentovich, M. O.; Katsaras, J. Deciphering Melatonin-Stabilized Phase Separation in Phospholipid Bilayers. *Langmuir* **2019**, *35*, 12236−12245.
(42) Ritwiset, A.; Khajonrit, J.; Krongsuk, S.; Rungrotmongkol, T. Molecular insight on the formation structure and dynamics of melatonin in an aqueous solution and at the water−air interface: A molecular dynamics study. *J. Mol. Liq.* **2021**, *108*, 107983.
(43) Benitez-King, G.; Hernandez, M. E.; Tovar, R.; Ramirez, G. Melatonin modulates microtubule organization in axons: implications for neuronal structure and function. *J. Pineal Res.* **2009**, *46*, 53−62.
(44) de Lima, G.; Faria, T.; Bastos, M. Hydration and conformational behavior of melatonin in aqueous solution: A FTIR and molecular modeling study. *J. Mol. Struct.* **2010**, *976*, 284−290.
(45) Engberg, O.; Saha Roy, D.; Krupa, P.; Banerjee, S.; Chaudhary, A.; Smith, A. A.; Li, M. S.; Maiti, S.; Huster, D. Molecules in the Serotonin−Melatonin Synthesis Pathway Have Distinct Interactions with Lipid Membranes. *J. Phys. Chem. B* **2025**, *129*, 2687−2700.
(46) Jove, M.; Mota-Martorell, N.; Pamplona, R. Melatonin and the physicochemical organization of biological membranes: implications for CNS function. *Front. Physiol.* **2023**, *14*, 1170083.
(47) Bolmatov, D.; Zav'yalov, D.; Zhernenkov, M.; Musaev, E. T.; Cai, Y. Q. Unified phonon-based approach to the thermodynamics of solid, liquid and gas states. *Ann. Phys.* **2015**, *363*, 221−242.
(48) Bolmatov, D. The phonon theory of liquids and biological fluids: Developments and applications. *J. Phys. Chem. Lett.* **2022**, *13*, 7121−7129.
(49) Bolmatov, D.; Collier, C. P.; Zav'yalov, D.; Egami, T.; Katsaras, J. Real space and time imaging of collective headgroup dipole motions in zwitterionic lipid bilayers. *Membranes* **2023**, *13*, 442.
(50) Dey, S.; Surendran, D.; Engberg, O.; Gupta, A.; Fanibunda, S. E.; Das, A.; Maity, B. K.; Dey, A.; Visvakarma, V.; Kallianpur, M.; Scheidt, H. A.; Walker, G.; Vaidya, V. A.; Huster, D.; Maiti, S. Altered membrane mechanics provides a receptor-independent pathway for serotonin action. *Chem.—Eur. J.* **2021**, *27*, 7533−7541.
(51) Collier, C. P.; Bolmatov, D.; Lydic, R.; Katsaras, J. Neuronal Plasma Membranes as Supramolecular Assemblies for Biological Memory. *Langmuir* **2025**, *41*, 2973−2979.
(52) Bolmatov, D.; Collier, C. P.; Katsaras, J.; Lavrentovich, M. O. Physical insights into biological memory using phospholipid membranes. *Eur. Phys. J. E* **2024**, *47*, 2.
(53) Lavrentovich, M. O.; Carrillo, J.-M. Y.; Collier, C. P.; Katsaras, J.; Bolmatov, D. Curvature Memory in Electrically Stimulated Lipid Membranes. *Langmuir* **2025**, *41*, 3157−3165.
(54) Bolmatov, D.; Zav'yalov, D.; Egami, T. Relaxor Ferroelectric-Like Spatiotemporal Memory in Field-Driven Lipid Bilayers. *Langmuir* **2026**, *42*, 2542−2547.
(55) Bolmatov, D.; Carrillo, J.-M. Y.; Sumpter, B. G.; Katsaras, J.; Lavrentovich, M. O. Double membrane formation in heterogeneous vesicles. *Soft Matter* **2020**, *16*, 8806−8817.

https://doi.org/10.1021/acschemneuro.5c00682
ACS Chem. Neurosci. XXXX, XXX, XXX−XXX